OTC 20293

Effect of Slide Deformation and Geometry on Waves Generated by Submarine Landslides: A Numerical Investigation

Kaushik Das, Steve Green, Debashis Basu, Ron Janetzke, and John Stamatakos, Southwest Research Institute®

This paper was prepared for presentation at the 2009 Offshore Technology Conference held in Houston, Texas, USA, 4–7 May 2009.

Abstract

The impact of slide deformation and geometry on surface waves generated by submarine landslides is studied using a computational model based on Navier-Stokes equations. The volume of fluid (VOF) method is used to track the free surface and shoreline movements. The Renormalization Group (RNG) turbulence model and the Detached Eddy Simulation (DES) multiscale model are used to simulate turbulence dissipation. Three-dimensional simulations are first compared with available experimental data involving the generation of waves by a rigid block sliding down an inclined plane. The role of slide deformation on the characteristics of the generated waves is evaluated. The results from the simulations are compared with the experimental data for the rigid slide. Simulated results highlight the importance and complexity of slide deformation on the generated wave characteristics and runup/rundown at various locations. Computed results also show the complex three-dimensional flow patterns in terms of the velocity field, shoreline evolution, and free-surface profiles. Predicted numerical results for time histories of free-surface fluctuations and the runup/rundown at various locations are found to be in good agreement with the available experimental data for the rigid slide. The location of the slide (whether it is fully submerged or aerial) also seems to influence the runup and wave height.

Introduction

Tsunamis are surface waves caused by the impulsive perturbation of the sea. Apart from co-seismic sea bottom displacement due to earthquakes, subaerial and submarine landslides can also produce localized tsunamis with large and complex wave runup. The wave characteristics and hazards related to tsunamis generated by submarine landslides have been an area of active research (Masson et al. 2006, Fine et al. 2005, Longva et al. 2003). Submarine landslides, which often accompany large earthquakes, can disturb the overlying water column as sediment and rock slump down slope. Any type of geophysical mass flow including debris flows, debris avalanches, landslides, and rockfalls can create submarine landslide-generated tsunamis. Earthquakes can also play an indirect role as the landslide-triggering mechanism. In addition to bringing devastating consequences and destruction to human lives, landslide-generated tsunamis constitute a threat in terms of direct wave impact or currents to offshore installations including oil platforms, risers, pipelines, and ships and to coastal installations. Coastal or shallow water structures are more prone to destruction due to higher wave current velocities in these places. Although the generation and propagation of earthquake-generated tsunamis have been studied for several decades and are now relatively well understood, such is not the case for landslide-generated tsunamis. While the mechanisms that generate these types of tsunami flows are generally understood, the ability to predict the flows they produce at coastlines still represents a formidable challenge due to the complexities of coastline formations and the presence of numerous coastal structures that interact and alter the flow. The generation and effects of landslide-generated tsunamis are complex and variable.

Theoretical approaches for solving the landslide-generated tsunami problem in three dimensions are extremely difficult to apply due to strong nonlinearities and the turbulence that develops from a breaking tsunami. Laboratory and analytical studies of tsunami water waves generated by submarine mass failure have been conducted by several authors (Heinrich 1992, Watts 2000, Enet et al. 2003). Other prior simulations of landslide-generated tsunamis (Liu et al. 2005, Grilli and Watts 1999, Lynett and Liu 2005, Rzadkiewicz et al. 1997) used models based on Navier-Stokes equations. These

analyses (Liu et al. 2005, Grilli and Watts 1999, Lynett and Liu 2005, Rzadkiewicz et al. 1997) either used two-dimensional Navier-Stokes simulations with a VOF-type free surface tracking or a multifluid finite element-based Navier-Stokes model (Rzadkiewicz et al. 1997) in which air and water motion were simulated. Most of the simulations were carried out in a two-dimensional framework. Jiang and LeBlond (1994), Imamura and Gica (1996), and Fine et al. (2005) used nonlinear shallow water wave equations. While most of the prior simulations focused on prediction of the impulse wave characteristics, none of them looked into the effect of slide deformation on the predicted wave characteristics and runup. Abadie et al. (2006) used a VOF interface tracking method to simulate submarine landslides and resulting wave generation. The computational domain in Abadie et al. (2006) was composed of three fluids: water, air, and the slide. The sliding wedge was represented by a Newtonian fluid of very large viscosity (~10^{10} Pa-s). By using this high viscosity value, the deformation of fluid particles within the slide followed a quasi-rigid behavior.

The present investigation evaluates the effect of slide deformation on impulse wave characteristics and runup/rundown at various locations. The Navier-Stokes equations are used to predict the submarine landslide movement and the subsequent generation and propagation of tsunami waves. Three-dimensional simulations are carried out for the Navier-Stokes equations; the flow solver FLOW-3D (Flow Sciences, 2006) is used. The VOF method is used in FLOW-3D to track the free surface and shoreline movement. The slide deformation is modeled through the use of a sediment scour model in FLOW-3D. In addition, the current analysis also evaluates the effect of the turbulence model on the flowfield. Turbulence is simulated using both the RNG-based turbulence model (Yakhot and Smith, 1992) and the multiscale DES (Basu, 2006) model. The DES model is implemented in the FLOW-3D solver and is based on the RNG-based turbulence model. The simulation results are validated against a benchmark experiment by Liu et al. (2005) involving a rigid aerial slide and generated waves. The experiment involved a three-dimensional, large-scale flume, in which a rigid wedge representing the slide moved down an inclined plane. The motion of the wedge, free surface, and runup were measured at different locations of the flume. The same three-dimensional sliding plane geometry is subsequently used, but the rigid slide is replaced by the deformable slide in the current work. In addition, a comparative study is also made in this paper regarding the effect of the slide position on the generated wave and predicted wave runup. Simulations are carried out with the rigid slide for both aerial slide and submerged slide configurations. Numerical results from the simulations are compared with experimental data for the time histories of free-surface fluctuations and the runup/rundown at various locations. The effect of slide deformation and the turbulence model on measured runup is also analyzed.

Solver Methodology

FLOW-3D (Flow Sciences, 2006) is a general purpose computational fluid dynamic simulation software package based on the algorithms for simulating fluid flow that were developed at Los Alamos National Laboratory in the 1960s and 1970s (Hirt and Nichols 1981, Harlow and Welch 1965, Welch et al. 1966). The basis of the solver is a finite volume or finite difference formulation, in Eulerian framework, of the equations describing the conservation of mass, momentum, and energy in a fluid. The code is capable of simulating two-fluid problems, incompressible and compressible flow, and laminar and turbulent flows. The code has many auxiliary models for simulating phase change, non-Newtonian fluids, noninertial reference frames, porous media flows, surface tension effects, and thermo-elastic behavior. FLOW-3D solves the fully three-dimensional transient Navier-Stokes equations using the Fractional Area/Volume Obstacle Representation (FAVOR) (Hirt and Sicilian 1985) and the volume of fraction (Hirt and Nichols 1981) method. The solver uses finite difference or finite volume approximation to discretize the computational domain. Most of the terms in the equations are evaluated using the current time-level values of the local variables in an explicit fashion, though a number of implicit options are available. The pressure and velocity are coupled implicitly by using the time-advanced pressures in the momentum equations and the time-advanced velocities in the continuity equations. It solves these semi-implicit equations iteratively using relaxation techniques. FAVOR (Hirt and Sicilian 1985) defines solid boundaries within the Eulerian grid and determines fractions of areas and volumes (open to flow) in partially blocked volume to compute flows corresponding to those boundaries. In this way, boundaries and obstacles are defined independently of grid generation, avoiding saw-tooth representation or the use of body-fitted grids. FLOW-3D has a variety of turbulence models for simulating turbulent flows, including the Prandtl mixing length model, one-equation model and two-equation k-ε model, RNG scheme, and a large eddy simulation (LES) model. The current simulations use the RNG model (Yakhot and Smith 1992). In addition, a multiscale DES turbulence model (Basu 2006) was implemented in FLOW-3D. Both the turbulence models are compared for their relative performance. The sediment scour model, which predicts the behavior of packed and suspended sediments, is used in the simulations involving deformable slide. The details of the sediment scour model are provided in subsequent sections.

RNG Turbulence Model

The RNG turbulence model solves for the turbulent kinetic energy (k) and the turbulent kinetic energy dissipation rate (ε). This RNG approach applies statistical methods for a derivation of the averaged equations for turbulent quantities, such as turbulent kinetic energy (k) and its dissipation rate. The RNG-based models rely less on empirical constants while setting a framework for the derivation of a range of parameters to be used at different turbulence scales. The RNG model uses equations similar to the equations for the k-ε model. However, equation constants that are found empirically in the standard

k-ε model are derived explicitly in the RNG model. Generally, the model has wider applicability than the standard k-ε one.

DES Multiscale Turbulence Model

The DES modeling approach differs from the Renolds Averaged Navier-Stokes (RANS) modeling approach by the eddy diffusivity closure. While the RANS closure models simulate the entire spectrum of turbulence, the DES variants allow some of the turbulence to be resolved explicitly, reducing the dependence on modeling. The DES formulations allow the reduction of eddy viscosity in the regions of interest, and fine scales are resolved. A switching function is used to activate the reduction in eddy viscosity. For the present simulations, a RNG-based DES multiscale turbulence model (Basu 2006) is implemented in FLOW-3D. The model is detailed in Basu (2006). In the DES model used, the switching function depends on both the local grid length as well as the turbulent length scale. A model constant C_b is also used to modify the eddy viscosity formulation. For the current simulations, the C_b value used is 0.1.

Sediment Scour Model

The sediment scour model available in FLOW-3D predicts the behavior of packed and suspended sediment. The model is detailed in the FLOW-3D manual (Flow Sciences 2006). The potential applications of this model include erosion around bridge piers, weirs, dams, and underwater pipelines and removal and drifting of sand or snow over terrain. The model consists of two basic components: drifting and lifting. Drifting acts on the sediment that is suspended in the flow; gravity (along with other body forces) causes the settling of the sediment. It is also based on the drift-flux model. In conjunction with the drifting and lifting models, a drag model is used to mimic the solidlike behavior of the sediment in regions where its concentration exceeds a cohesive solid fraction. The viscosity and density are functions of the sediment concentration, and they are calculated as a function of the sediment concentration. In the current simulations, the deformable slide is represented by suspended and packed sediment as dictated by the local flow field and sediment concentration distribution. The suspended sediment advects and drifts with the fluid due to the influence of the local pressure gradient. The packed sediment, which does not advect, represents sediment that is bound by neighboring sediment particles. Packed sediment can only move if it becomes eroded into suspended sediment at the packed sediment-fluid interface. Suspended sediment can become packed sediment if the fluid conditions are such that the sediment drifts toward the packed bed more quickly than it is eroded away.

The sediment concentrations are stored as units of mass/volume. The solid volume fraction f_s is a measure of the fraction of the total volume that is occupied by the sediment. The solid fraction f_s is used for the viscosity and drag models. The mean fluid viscosity is enhanced by the suspended sediment. This enhancement rises with sediment concentration until the solid volume fraction reaches the cohesive solid fraction $f_{s,co}$. Further rises in sediment concentration beyond solid volume fraction $f_{s,co}$ do not cause the viscosity to rise; rather, the particles begin to interact with one another to cause solidlike behavior. The solidlike behavior is predicted by imposing a linear drag term to the momentum equation. The viscosity is given by

$$\mu^* = \mu_f \left(1 - \frac{\min(f_S, f_{S.co})}{f_{s,cr}} \right)^{-1.55} \quad (1)$$

where μ_f is the molecular viscosity of the liquid, μ^* is the average viscosity of the mixture, and $f_{s.cr}$ is the critical solid fraction. The critical solid fraction is the solid fraction at which the sediment particles are completely bound together in a solidlike mass. The deformable slide in the current simulations uses the above formula to calculate viscosity.

Experiment

The experiment on the sliding wedge wave tank was conducted at Oregon State University (Liu et al. 2005). The wave tank has a length of 104 m, a width of 3.7 m, and a depth of 4.6 m. A plane slope (a beach with an inclination of two horizontal to one vertical) was located near one end of the tank and a dissipating beach at the other end. For all experiments, the water depth in the wave tank was about 2.44 m. The landslide was represented by a sliding wedge. The sliding wedge moved down the slope by gravity, rolling on specially designed v-shaped wheels (with low friction bearings) that ride on aluminum strips with shallow grooves inset into the slope. Figs. 1 and 2 show the experimental setup and the wedge used. Fig. 3 shows the schematic sketch of the experiment and the nomenclature used in the experiments. The length of the wedge (b) is 91.44 cm; a front face dimension (a) is 45.72 cm high. In Fig. 3, the distance x is measured seaward from the intersection of the seawater level (SWL) with the slope. The runup, R, is measured vertically from the SWL, and Δ is the vertical distance from the SWL to the highest point measured positively upward from the SWL. In the experiment, a sufficient number of wave gauges were used to determine the seaward-propagating waves (the waves propagating to either side of the sliding bodies). The experimental setup uses an initially aerial rigid slide. However, most of the simulations in the current work used a submerged slide. One set of simulations was initially carried out with an aerial slide to evaluate the influence of slide position on the wave runup and height.

Computational Details

A three-dimensional flow domain representing the experiment setup described by Liu et al. (2005) was defined within the framework of the FLOW-3D software. The entire flow domain is 21 m in length, 3.8 m in height, and 3.7 m in width. A vertical cross section in the midplane of the flow field near the wedge-shaped wave generator is shown in Fig. 5. Fig. 4 shows the initially submerged landslide. The ramp in these experiments has a 2:1 slope, and the wedge is placed so that its leading edge is initially at the undisturbed water surface. The water depth is specified as 3.3 m, so the ramp extends 6.6 m down the length of the flow domain. The wedge-shaped block (either solid or initial deformable material) representing the landslide material is 0.5 m high and 0.653 m wide and is placed symmetrically between the front and back walls of the channel. The coordinate system for these simulations has its origin where the water surface meets the ramp and all surface elevations are referenced to the initial undisturbed water level. Fig. 6 shows the initial fluid configuration for the aerial slide. In this configuration, the wedge is placed so that its leading edge is initially at the undisturbed water surface.

A nonuniform grid comprising a mesh of 70 × 60 × 51 cells in the x, z, and y directions respectively was defined for these simulations. Note that the grid also covers the initial air space above the water to accommodate the block motion and the surface waves. This feature is required in the FLOW-3D software as part of its VOF free-surface tracking algorithm. The finest grid spacing was at the leading edge of the ramp. At this location, the grid spacing is 0.0196 m in the z direction and 0.0391 m in the x direction. The grid expanded from the origin in both these directions, but the main area of interest between the leftmost wall and the bottom of the ramp is covered by a mesh of 60 × 60 cells in the x and z directions. The y direction grid spacing was uniform at 0.07 m over the entire flow domain. By forming the computational mesh in this way, adequate resolution was provided in the ramp region while ensuring that reflections from the downstream wall did not interact with the ramp during the timeframe of interest.

All boundary surfaces of the flow domain and the ramp were defined as nonslip smooth walls. Similarly, for the simulations of solid wedge motion, the faces of the wedge were also smooth nonslip surfaces. For the solid wedge cases, the wedge motion follows a specified velocity profile that approximates the measured time history of the wedge as described by Liu et al. (2005). The prescribed time history of the wedge speed is described in Fig. 6. For the deformable wedge cases, the particle bed deformation and flow follows the sediment scour modeling provisions in FLOW-3D as described previously. The fluid in the channel was specified as water with a density of 1000 kg/m^3 and a viscosity of 1 cP. In these simulations, the air above the fluid surface is modeled as empty space that did not interact with the water. Laminar flow conditions prevail over most of the flow domain except near the moving slide. Simulations were conducted where laminar-only conditions were imposed over the entire flow field and where turbulent flow was modeled where required. For the turbulent flow cases, both a standard RNG model and an RNG model enhanced with multiscale DES were used to capture any turbulence effects near the moving wedge. For the present simulations, the pressure-based solver was chosen along with the implicit algorithm. The viscous stress was computed using an explicit scheme. For the advection equations, an explicit scheme was used. A second-order central difference scheme was used for the momentum equations.

Results and Discussions

Computational results are presented for the Navier-Stokes simulations and for different turbulence models. Presented results include the unsteady fluid configurations' sediment motion at different times and comparison of the predicted water surface height and elevation for different turbulence models and simulation cases. The effect of slide geometry and the turbulence model constants on the predicted solution are also shown. The simulations with the submerged slide were compared with the aerial slide in terms of runup and wave height and flowfields.

Fig. 7 shows the time-dependent evolution of the flowfield for the simulation of the solid block motion with the submerged slide. The initial wave is shown at t=0.6 sec when the wave trough is at its lowest point. The front of this wave begins to travel downstream, and the back of the wave breaks backward over the top of the wedge. At t=1.0 sec, the second wave is just being formed as a result of the continued wedge motion and the reflection of the back of the initial wave from the ramp. The initial and second waves disperse laterally, and their heights quickly decrease. The configuration at time t=2.0 sec shows the initial runup wave at its maximum extent up the slope. A large wake trailing the moving block can be observed at t=2.0 sec. This shows the extent of the bluff body effects. Finally, the flowfield at t=3.0 sec shows the flow at the time just after the block motion is halted. Note that waves continue to move along the surface and the vortex behind the block is beginning to move downstream away from the block.

There are subtle but significant differences between the flow fields generated from a submerged landslide and an aerial landslide. Snapshots of the midplane of the flow field generated by an aerial landslide are shown in Fig. 8. This simulation is identical to that depicted in Fig. 7, except that the block starts above the water surface. This configuration is similar to the experiment of Liu et al. (2005). Note that the block is just submerged at t=0.8 sec where a wave is generated from the front of the block as it is entering the water. The instantaneous flowfield at t=1.2 sec shows the formation of maximum trough behind the block. This trough and the amount of water involved in the initial wave are more extensive than that shown in Fig. 7 for the submerged landslide. This can be attributed to the bluff body effect for the submerged landslide. The generation of the second wave from the aerial landslide is shown at t=1.6 sec. This is similar to that shown in Fig. 7 for

the submerged landslide; however, a larger volume of water is affected by the aerial landslide than for the submerged landslide. Finally, the fluid state at the time of the maximum runup from the aerial landslide is shown at t=2.8 sec. Comparing Fig. 7 to Fig. 8, shows that this runup is greater than for the aerial landslide than for the submerged landslide.

Fig. 9 shows the snapshots of velocity vectors on the centerline vertical plain for the aerial sliding wedge from the three-dimensional LES results of Liu et al. (2005). Comparing Figs. 8 and 9, shows a qualitative agreement between the current simulations with the aerial landslide and the LES results of Liu et al. (2005). Even though the simulations by Liu et al. (2005) used LES and a much larger grid compared to the current simulations, the present simulations show good agreement with their results.

The simulated motion of the bed during the deformable landslide event is summarized in a series of five instantaneous flowfields in Fig. 10. These simulations were obtained with the sediment scour model. The figure shows the evolution of the landslide mass as it moves down the slope. The figure at t=0 sec shows the initial configuration of the bed similar to the view of the solid block in Fig. 8. At a simulated time of 0.4 sec, the bed has slumped and the trough of the initial runup wave is at its maximum behind the bed. Although the figure at t=1.4 sec does not distinguish between the bed types, the simulation shows that the bed has started to separate into the three types allowed by the model. A packed bed resulting from the slump of the initial bed is near the initial bed position. A suspended bed has flowed almost halfway down the ramp. Finally, there is a dispersed phase as a result of the lifting of particles from the denser material that is too dilute to be observed in these images. The figure at t=4.6 sec shows further separation of the bed types, and the simulation shows that the packed bed is moving by continuous erosion and redeposition down the slope. Finally, the snapshot at t=8.0 sec shows the bed being reformed at the bottom of the slope. In summary, these simulations show that a fast moving portion of the bed reaches the bottom of the slope well ahead of the rest of the initial mass, but all of the initial bed eventually settles at the bottom the slope and the plain near the foot of the slope. Comparing Fig. 10 with Figs. 7 and 8, shows a distinct difference in the free surface profiles between the rigid slide and the deformable slide. For the sediment scour model simulations with the deformable slide, the runup is much less compared to the simulations with the rigid slide. It clearly shows that the bluff body effect significantly influences the wave runup and height.

The total effective dynamic viscosity (*i.e.*, fluid viscosity plus eddy viscosity) for the RNG and DES models of the solid wedge motion are compared in Fig. 11. The area with significant generation of eddy viscosity is larger for the RNG turbulence model compared to the DES turbulence model. Furthermore, the eddy viscosity values for the RNG model are approximately an order of magnitude greater than in the DES model. This is expected because the DES model allows eddy viscosity to be reduced in proportion to the local grid length and turbulence. This helps resolve the dynamic structures of the flowfield. Both simulation cases with RNG and DES models show that there is significant turbulence generated as the landslide moves through the fluid. The distribution of the suspended sediment for the RNG and DES simulations of the deformable landslide mass is compared in Fig. 12. The overall movement of the sediment in both these simulations cases is similar, but the sediment moves more quickly down the ramp with the DES model than in the RNG case. Figs. 11 and 12 clearly show that the DES model predicts a more localized interaction between the landslide mass and the surrounding fluid than the RNG model. In addition, the landslide mass is predicted to have a greater velocity under the effects of the DES model than for the RNG model.

The wave runups behind the landslide predicted by all the simulations performed here are compared in Fig. 13. Note that the runups for all the simulations of the solid wedge are in close agreement with each other; similarly, the runup predicted by all the simulations of the deformable mass are also in close agreement with each other. Overall, the solid mass gives greater runup average amplitudes because of the bluff body effects for the flow behind the wedge. Note that in spite of the differences in the near-field effects predicted using the laminar-only assumption and the two different turbulence models, there is little difference in the simulated surface wave motion. This suggests that it is not necessary to model turbulence effects for predicting tsunami runup. Conversely, if the risk to marine equipment near the path of the landslide is of interest, then turbulence effects could play a significant role.

Fig. 14 shows comparison of the time history of the runup waves for the aerial and submerged landslides. The simulations are compared with the experimental data of Liu et al. (2005). The measurements extend only to a time of 4 sec, but the simulation results for the aerial landslide agree well with the measured values. Note that, overall, the time history of the runup wave heights is similar. The events in the runup wave for the aerial landslide lag those of the submerged landslide as expected. The runup wave heights for the aerial landslide are greater than those of the submerged landslide as described above.

Conclusions

Three-dimensional Navier-Stokes simulations were carried out to model tsunami wave generation by submarine landslides. The effect of slide deformation on the generated wave is also analyzed. In addition, the influence of the slide position (aerial or submerged) on the generated wave and runup is also investigated. The sediment scour model is used to model slide deformation. Both rigid and deformable slides were used to analyze the influence of the slide shape on the flowfield. Computed results showed that rigid slides produce more turbulence as well as greater wave runup and wave height. The bluff body effect of rigid landslides seems to significantly influence the wave height and runup. The DES turbulence model constant seems to influence the eddy viscosity and results in a lower value of eddy viscosity. The details of the flow

turbulence do not greatly affect the far field effects such as wave height and runup. In the near field, however, turbulence appears to play a stronger role. Accurate prediction of turbulence may be more important in determining how the landslide material spreads after the event and results in postevent damage to coastal areas and offshore structures. The events in the runup wave for the aerial landslide lag those of the submerged landslide. The runup wave heights for the aerial landslide are greater than those of the submerged landslide due to the bluff body effect. The computational tool developed to predict landslide-generated tsunamis during this investigation has great application to oil and gas industries, especially for oil exploration regions and offshore structures. This developed computational tool can help provide inputs to assess risk from landslide-generated tsunamis for near shore as well as offshore structures. Landslide type and characteristics can significantly influence the generated tsunami and affect the marine equipment as well as offshore structures.

Acknowledgments

The work was sponsored by the Advisory Committee for Research at Southwest Research Institute® through an Internal Research and Development Project. The authors acknowledge the useful discussions provided by the technical support staff from Flow Sciences, Inc., and the help from Sharon Odam at the Geosciences and Engineering Division in preparing the manuscript.

References

Abadie, S., Grilli, S., and Glockner, S. 2006. A Coupled Numerical Model for Tsunami Generated by Subaerial and Submarine Mass Failures. *Proc*., 30th Internation Conference on Coastal Engineering, San Diego, California, 1420-1431.

Basu, D. 2006. Hybrid Methodologies for Multiscale Separated Turbulent Flow Simulations. PhD Dissertation, University of Cincinnati, Cincinnati, Ohio.

Enet, F., Grilli, S.T., and Watts, P. 2003. Laboratory Experiments for Tsunamis Generated by Underwater Landslides: Comparison with Numerical Modeling. *Proc.*, 13th Offshore and Polar Engineering Conference, Cupertino, California, International Society of Offshore and Polar Engineers, **3**: 372-379.

Flow Sciences Incorporated. 2006. Flow-3D Users Manual, Version 9.1. Santa Fe, New Mexico: Flow Sciences Incorporated.

Fine, I.V., Rabinovich, A.B., Bornhold, B.D., Thomson, R.E., and Kulikov, E.A. 2005. The Grand Banks Landslide-Generated Tsunami of November 18, 1929: Preliminary Analysis and Numerical Modeling. *Marine Geology* **203**: 201–218.

Grilli, S.T. and Watts, P., 1999. Modeling of Waves Generated by a Moving Submerged Body, Applications to Underwater Landslides. *Engineering Analysis with Boundary Elements* **23**: 645–656.

Harlow, F.H. and Welch, J.E. 1965. Numerical Calculation of Time-Dependent Viscous Incompressible Flow. *Physics of Fluid* **8**: 2182–2189.

Heinrich, P. Nonlinear Water Waves Generated by Submarine and Aerial Landslides. *Journal of Waterway, Port, Coastal and Ocean Engineering* **118** (3): 249-266.

Hirt, C.W. and Nichols, B.D. 1981. Volume of Fluid (VOF) Method for the Dynamics of Free Boundaries. *Journal of Computational Physics* **39**: 201–225.

Hirt, C.W. and Sicilian, J.M. 1985. A Porosity Technique for the Definition of Obstacles in Rectangular Cell Meshes. *Proc*., Fourth International Conference on Ship Hydrodynamics, Washington, DC, National Academy of Sciences, 1–19.

Imamura, F. and Gica, E.C. 1996. Numerical Model for Tsunami Generation Due to Subaqueous Landslide Along a Coast. *Science of Tsunami Hazards* **14**: 13–28.

Jiang, L. and LeBlond, P.H. 1994. Three-Dimensional Modeling of Tsunami Generation Due to a Submarine Mudslide. *Journal of Physical Oceanography* **24**: 559–573.

Liu, P.L.-F., Wu, T.-R., Raichlen, F., Synolakis, C.E., and Borrero, J.C. 2005. Runup and Rundown Generated by Three-Dimensional Sliding Masses. *Journal of Fluid Mechanics* **536**: 107–144.

Longva, O., Janbu, N., Blikra, L.H., and Boe, R. 2003. The Finneidfjord Slide: Seafloor Failure and Slide Dynamic. In *Submarine Mass Movements and Their Consequences*, ed. J. Locat and J. Mienert, 531–538. Dordrecht, Netherlands: Kluwer Academic Publishers.

Lynett, P. and Liu, P.L.-F. 2005. A Numerical Study of the Runup Generated by Three-Dimensional Landslides. *Journal of Geophysical Research* **110** (03006): doi:10.1029/2004JC002443.

Masson, D.G., Harbitz, C.B., Wynn, R.B., Pedersen, G., and Lovholt, F. 2006. Submarine Landslides: Processes, Triggers and Hazard Prediction. *Philosophical Transaction of the Royal Society* **364**: 2009–2039.

Rzadkiewicz, A.S., Mariotti, C., and Heinrich, P. 1997. Numerical Simulation of Submarine Landslides and Their Hydraulic Effects. *Journal of Waterway, Port, Coastal, and Ocean Engineering* **123** (4): 149–157.

Watts, P. 2000. Tsunami Features of Solid Block Underwater Landslides, *Journal of Waterway, Port, Coastal and Ocean Engineering* **124** (3): 144–152.

Welch, J.E., Harlow, F.H., Shannon, J.P., and Daly, B.J. 1966. The MAC Method: A Computing Technique for Solving Viscous, Incompressible, Transient Fluid Flow Problems Involving Free-Surfaces. Los Alamos Scientific Laboratory Report LA-3425.

Yakhot, V. and Smith, L.M. 1992. The Renormalization Group, the e-Expansion and Derivation of Turbulence Models. *Journal of Scientific Computing* (7): 35–61.

Fig. 1. Wedge used in the Oregon State University experiments (Liu et al. 2005)

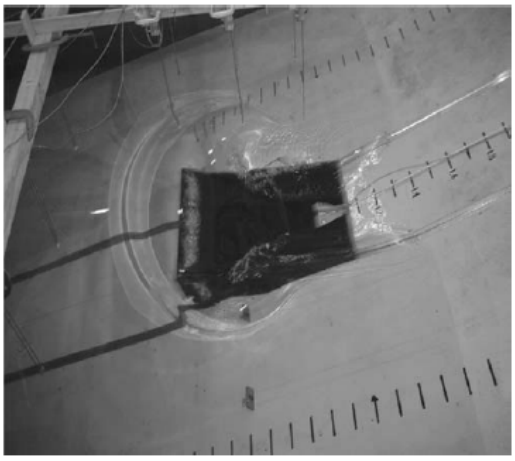

Fig. 2. Wedge sliding down during the large-scale experiment at Oregon State University (Liu et al. 2005)

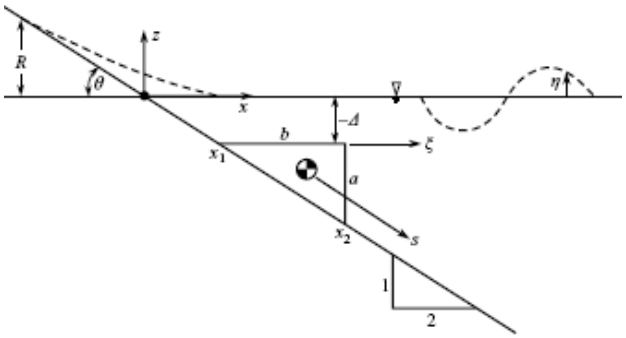

Fig. 3. A schematic of the experimental setup used in the experiment at Oregon State University (Liu et al. 2005) and the associated nomenclature

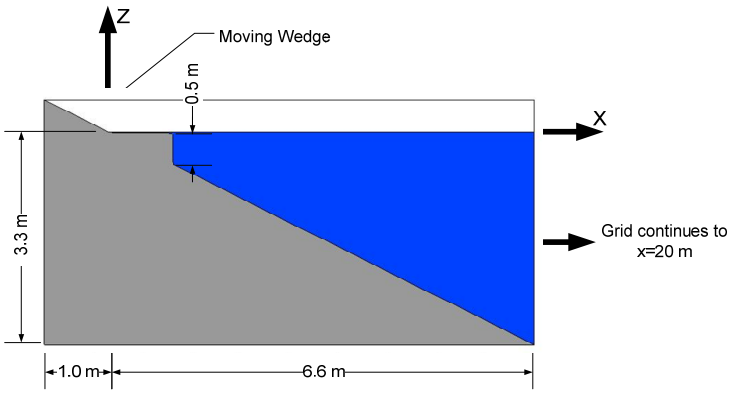

Fig. 4. Flow domain and initial fluid configuration used in the simulations for the submerged landslide

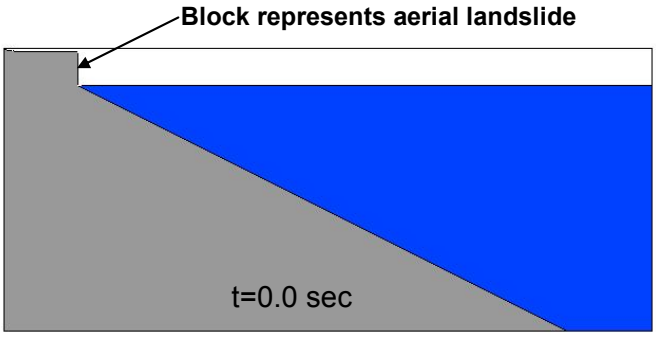

Fig. 5. Flow domain and initial fluid configuration used in the simulations for the aerial landslide

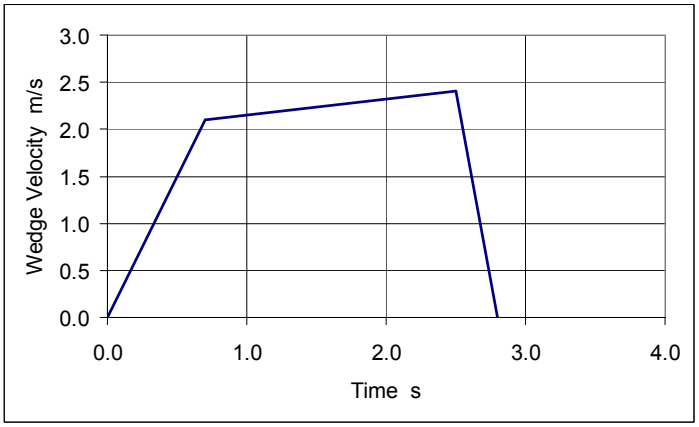

Fig. 6. Prescribed velocity for the sliding block

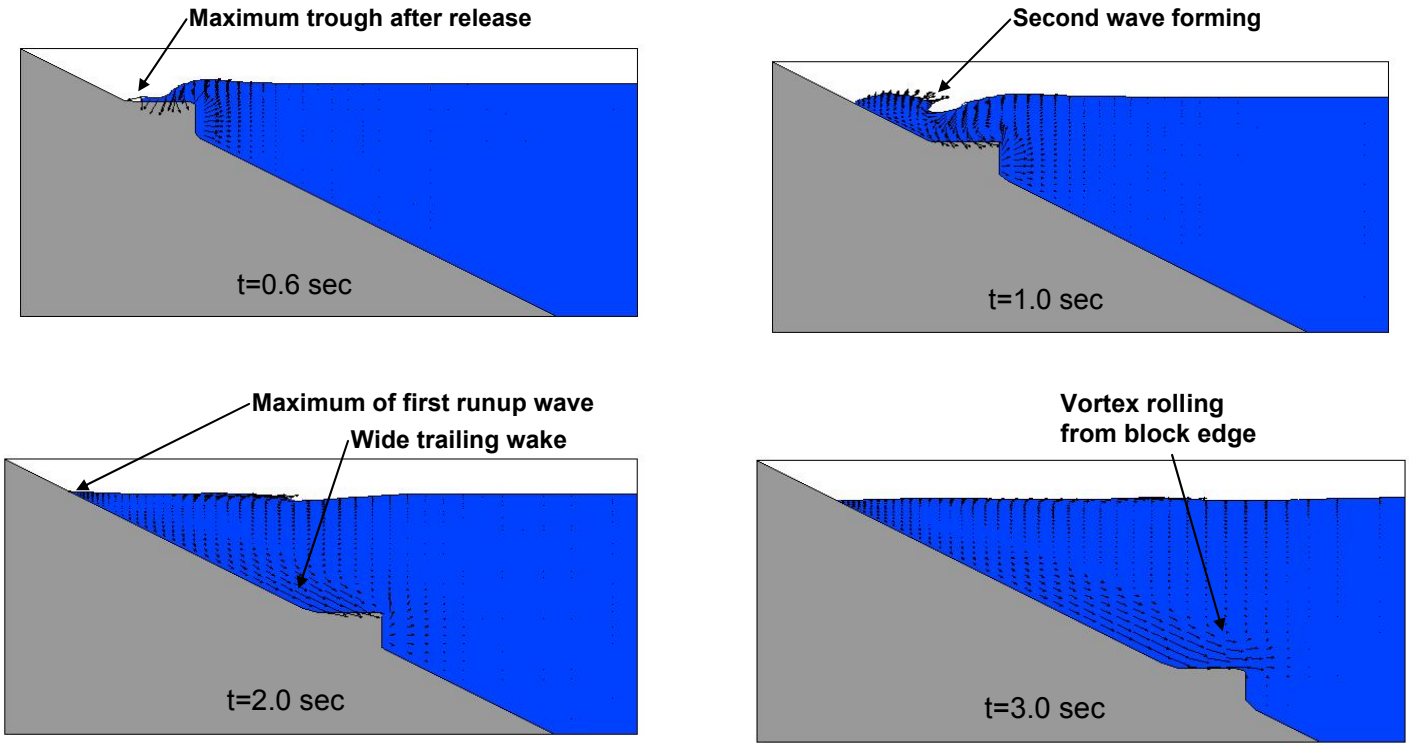

Fig. 7. Fluid configuration at different times in the Navier-Stokes simulations for the submerged landslide

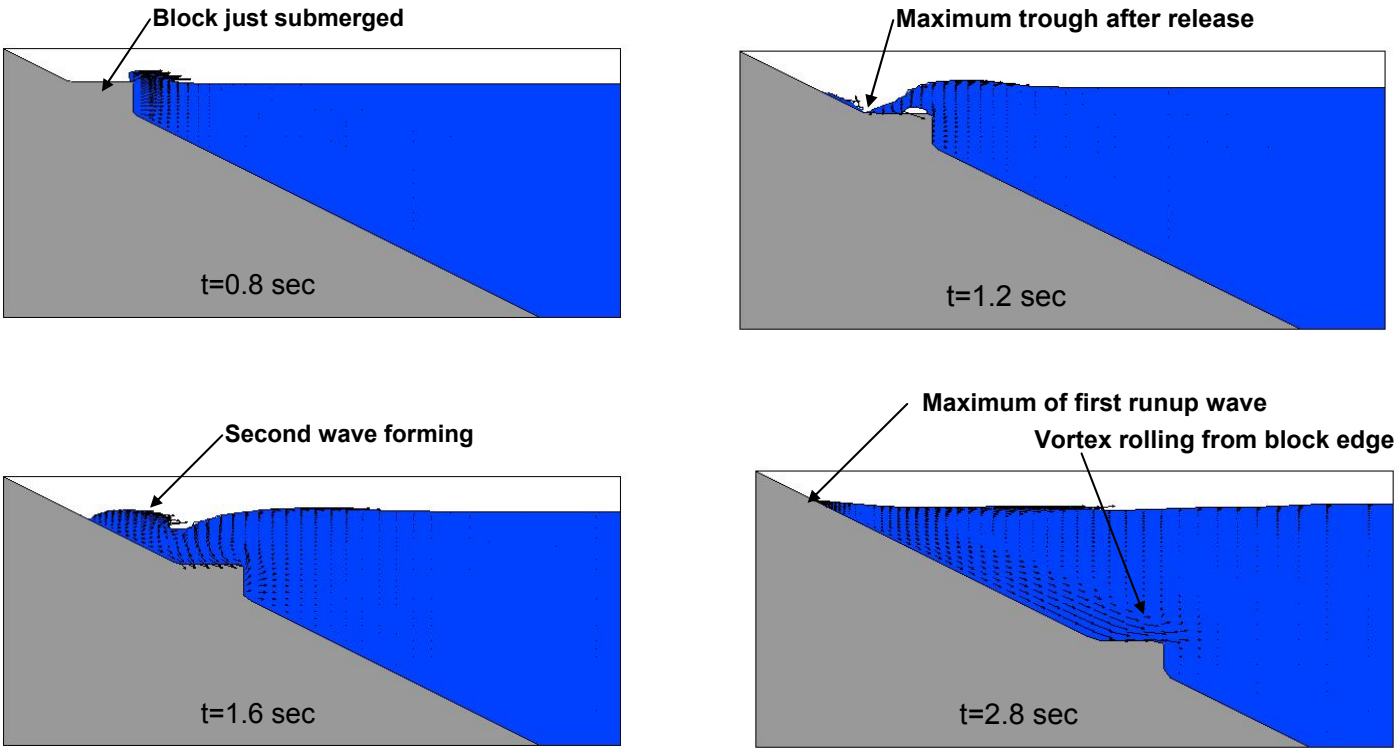

Fig. 8. Fluid configuration at different times in the Navier-Stokes simulations for the partial aerial landslide

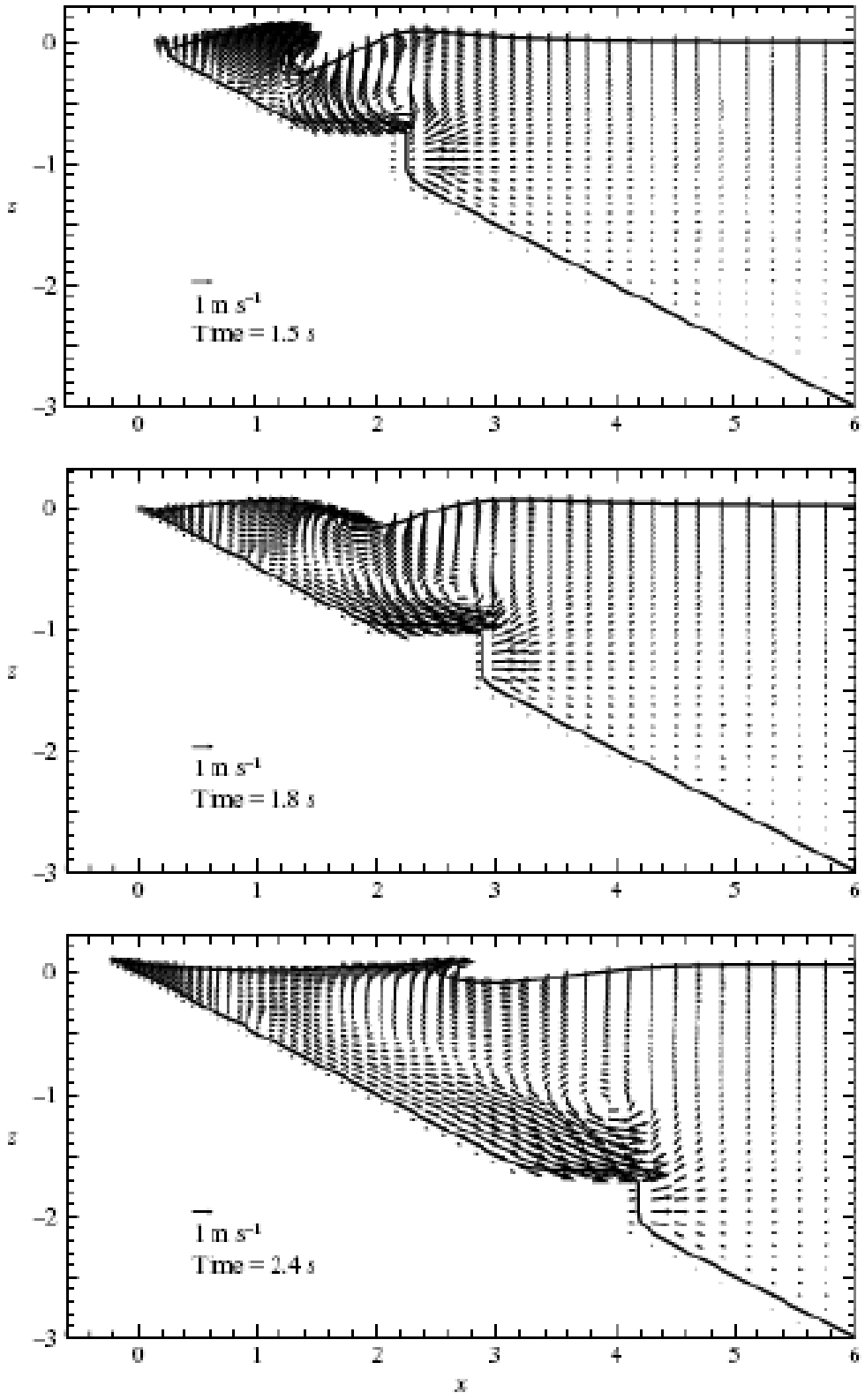

Fig. 9. Fluid configuration at different times in the Navier-Stokes simulations of Liu et al. (2005)

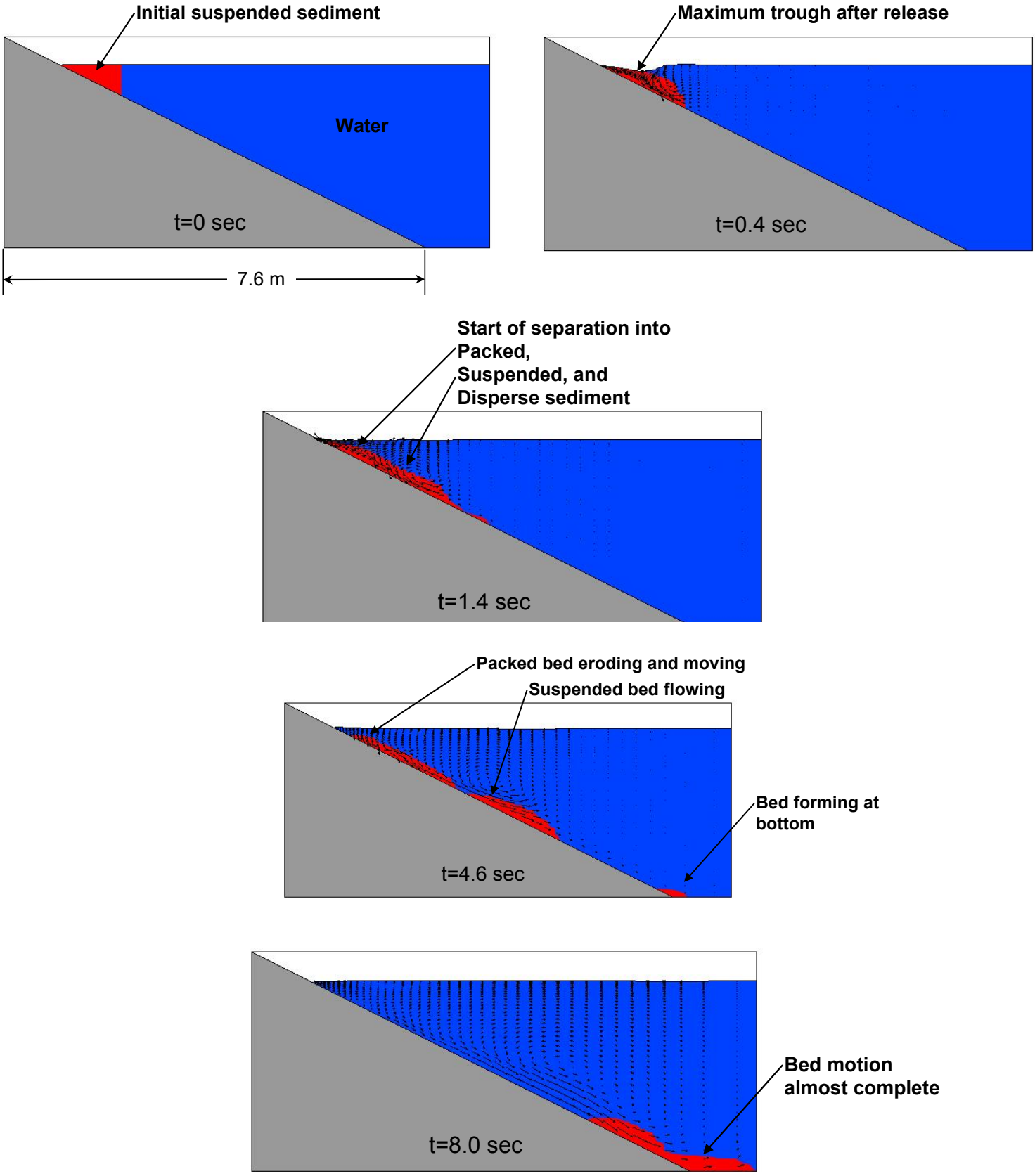

Fig. 10. Time snapshots of sediment (deformable slide) motion in the Navier-Stokes simulations

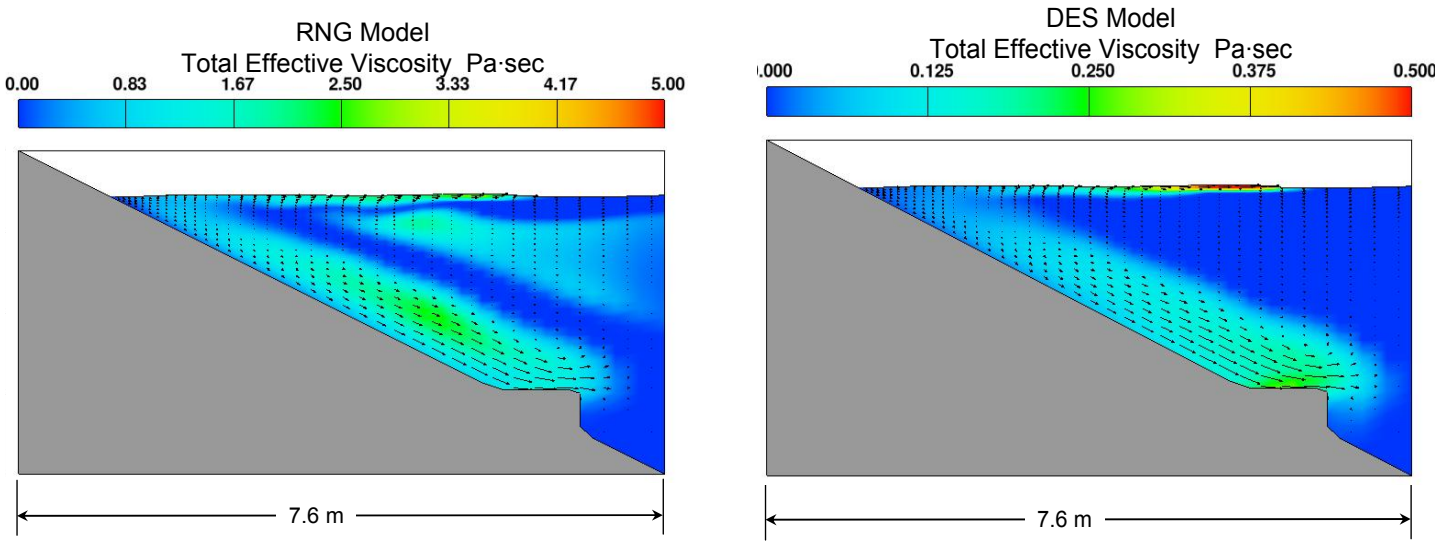

Fig. 11. Dynamic viscosity contours for the rigid slide with RNG and DES models

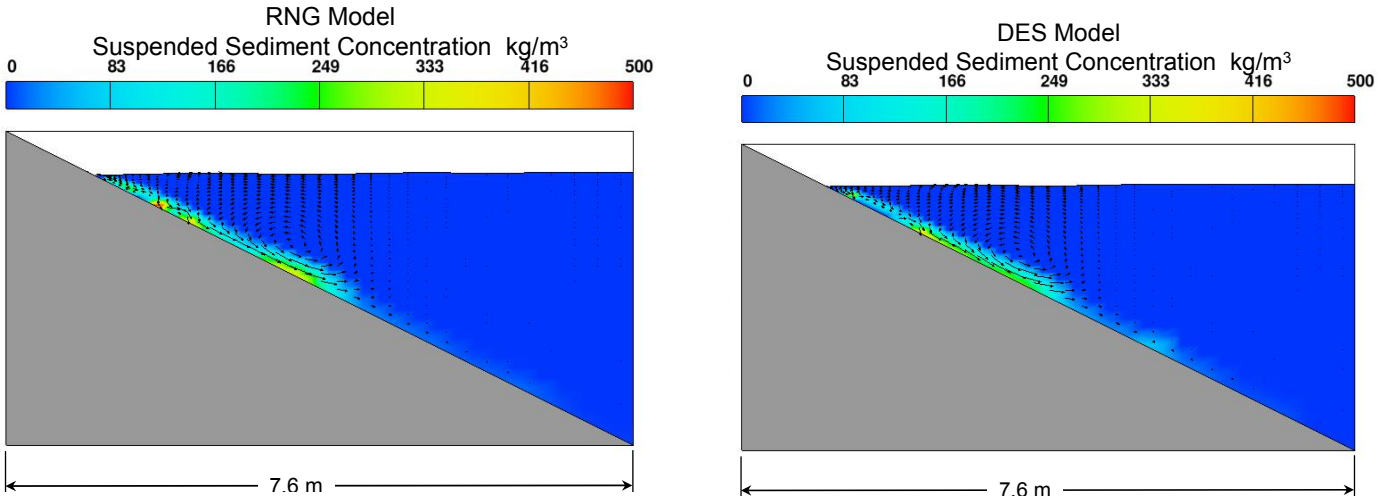

Fig. 12. Suspended sediment concentrations for the deformable slide with RNG and DES models

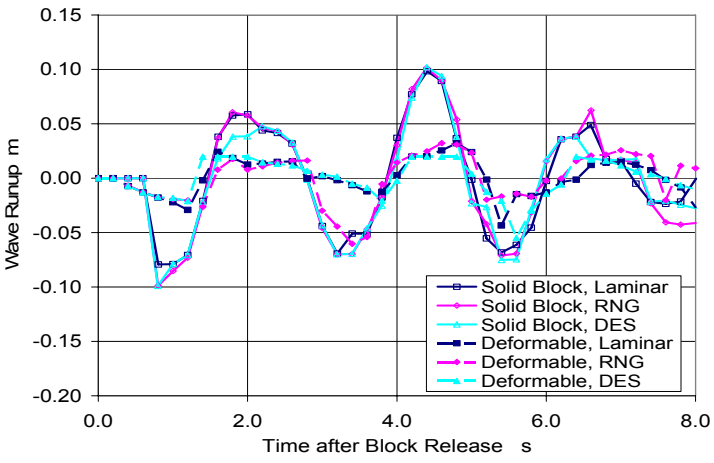

Fig. 13. Wave runup comparisons for different cases

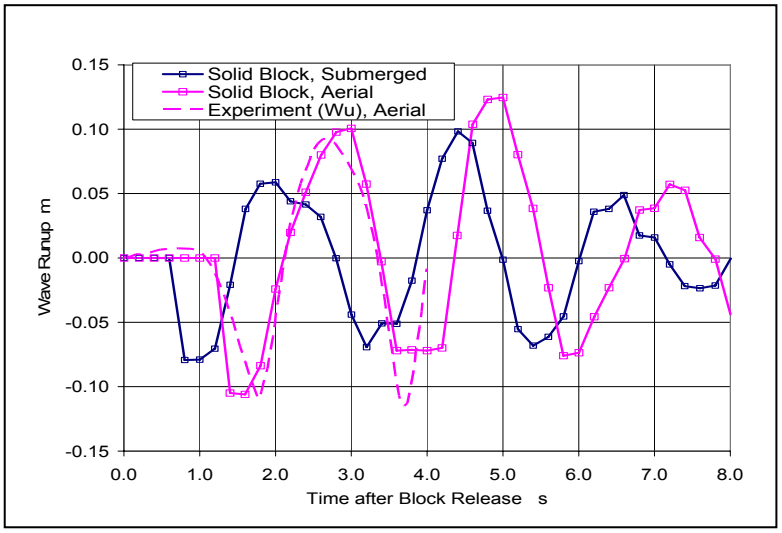

Fig. 14. Wave runup comparisons for submerged and aerial slides